Interface Manipulations Using Cross-Linked Underlayers and Surface-Active Diblock Copolymers to Extend Morphological Diversity in High-χ Diblock Copolymer Thin Films

Noémie Baumgarten, Muhammad Mumtaz, Daniel Hermida Merino, Eduardo Solano, Sami Halila, Julien Bernard, Eric Drockenmuller, Guillaume Fleury, Redouane Borsali

Interface Manipulations Using Cross-linked Underlayers and Surface Active Diblock Copolymer to Extend Morphological Diversity in High-χ Diblock Copolymer Thin Films

Noémie Baumgarten,[1] Muhammad Mumtaz,[2] Daniel Hermida Merino,[3,4] Eduardo Solano,[5] Sami Halila,[2] Julien Bernard,[1] Eric Drockenmuller,[1,] Guillaume Fleury,[6,*] and Redouane Borsali[2,*]*

[1)] Univ Lyon, Université Lyon 1, INSA de Lyon, CNRS, Ingénierie des Matériaux Polymères, UMR 5223, F–69003, Lyon, France

[2)] Univ Grenoble Alpes, CNRS, CERMAV, F-38000 Grenoble, France

[3)] Dutch-Belgian Beamline, Netherlands Organization for Scientific Research, European Synchrotron Radiation Facility, F-38000 Grenoble, France

[4)] Departamento de Física Aplicada, CINBIO, Universidade de Vigo, Campus Lagoas-Marcosende, E36310 Vigo, Galicia, Spain

[5)] NCD-SWEET Beamline, ALBA Synchrotron Light Source, 08290 Cerdanyola del Vallès, Spain

[6)] Univ. Bordeaux, CNRS, Bordeaux INP, LCPO, UMR 5629, F-33600, Pessac, France

Corresponding authors E-mails: eric.drockenmuller@univ-lyon1.fr

guillaume.fleury@u-bordeaux.fr

redouane.borsali@cermav.cnrs.fr

KEYWORDS: High-χ diblock copolymers, cross-linked statistical copolymers, thin films, fluorinated surface-active polymer, grazing-incidence small-angle X-ray scattering, microwave solvent vapor annealing

ABSTRACT: Top and bottom interfaces of high-χ cylinder-forming polystyrene-block-maltoheptaose (PS-*b*-MH) diblock copolymer (BCP) thin films are manipulated using cross-linked copolymer underlayers and a fluorinated phase preferential surface active polymer (SAP) additive to direct the self-assembly (both morphology and orientation) of BCP microdomains into sub_10nm patterns. A series of four photo-cross-linkable statistical copolymers with various contents of styrene, 4-vinylbenzyl azide cross-linker and a carbohydrate-based acrylamide are processed into 15 nm thick cross-linked passivation layers on silicon substrates. A partially fluorinated analogue of PS-*b*-MH phase preferential SAP additive is designed to tune the surface energy of the top interface. The self-assembly of PS-*b*-MH thin films on top of the different cross-linked underlayers and including 0-20 wt% of SAP additive is investigated by Atomic Force Microscopy and Synchrotron Grazing Incidence Small Angle X-Ray Scattering. The precise manipulation of the interfaces of ca. 30 nm thick PS-*b*-MH films not only allows to control the in-plane/out-of-plane orientation of hexagonally packed (HEX) cylinders but also promotes epitaxial order-order transitions from HEX cylinders to either face-centered orthorhombic or body-centered cubic spheres without modifying the volume fraction of both blocks. This general approach paves the way to the controlled self-assembly of other high-χ BCP systems.

INTRODUCTION

The self-assembly of block copolymers (BCP) thin films is a promising bottom-up approach able to support classical top-down photolithography processes to reach devices with increasingly smaller feature dimensions.[1-5] BCP thin films with well-ordered nanoscale periodic patterns have been used as lithographic masks after removal of a sacrificial block to produce semi-conductors,[6] integrated circuits,[7] bit-patterned media,[8] magnetic dot arrays,[9] resistive memories,[10] filtration membranes,[11] photovoltaic cells,[12] or photonic materials.[13] Most of these applications require well-ordered microdomains oriented perpendicular to the substrate and spreading over large areas. In the bulk state, the volume fraction of the blocks (f), the total degree of polymerization (N) and the Flory-Huggins interaction parameter (χ) dictate the morphology and dimensions of the self-assembled microdomains. In thin films, additional parameters such as commensurability between the BCP period and film thickness, preferential interactions at one or both interfaces and annealing conditions, strongly impact the self-assembly.[14] Accordingly, the self-assembly of lamellar- or cylinder-forming BCPs in thin films often affords the formation of in-plane structures due to the preferential interactions between one of the blocks and the substrate.[14] Several methods have been used to direct the BCP microdomains orientation in thin films: *e.g.* solvent vapor annealing (SVA),[15] zone annealing,[16] graphoepitaxy,[17] chemoepitaxy,[18] shear forces,[19] application of electric or magnetic fields,[20] as well as directional solidification.[21] In the late 90s, Russell, Hawker and coworkers pioneered substrate neutralization using covalently-grafted poly(styrene-*stat*-methyl methacrylate) (PS-*s*-PMMA) brushes to overcome the preferential interaction of PMMA with the silicon substrate and to promote perpendicular orientation of PS-*b*-PMMA lamellae in thin films.[22] The orientation control of PS-*b*-PMMA microdomains has been further extended using mixtures of homopolymer brushes,[23] and pseudo-brushes.[24] Homopolymer and BCP brushes have also been applied to control the orientation of polystyrene-*b*-poly(*L*-lactide), polystyrene-*b*-

poly(ethylene oxide) (PS-*b*-PEO) and polystyrene-*b*-poly(2-vinyl pyridine) (PS-*b*-P2VP) microdomains.[23,25,26] Neutral copolymer mats (*i.e*. cross-linked underlayers for the controlled orientation of BCP structure) obtained by thermal cross-linking of benzocyclobutene-functionalized PS-*r*-PMMA were further developed by Hawker, Russell and coworkers to circumvent the substrate-dependent chemistry inherent to covalently-grafted (co)polymer brushes.[27] Neutral cross-linked underlayer analogues were obtained by thermal or photo-chemical cross-linking of PS-*r*-PMMA copolymers carrying azide,[28] epoxy,[29] or ketene[30] functionalities as well as by UV-irradiation of polystyrene coatings.[31] Rather than manipulating comonomer mixtures representative of the PS and PMMA blocks, and coping with a compositional drift inherent to their copolymerization process, Ellison, Willson and coworkers reported a library of cross-linked underlayers obtained from statistical copolymers and homopolymers obtained exclusively from styrenic (co)monomers, *i.e.* different *para*-substituted styrenes and 4-vinylbenzyl azide as photo-cross-linkable group.[32] Alternatively, SVA has been developed to overcome the low effectiveness of thermal annealing for some BCPs especially those having comparable glass transition and degradation temperatures. SVA imparts chain mobility by plasticization with solvent molecules and has for instance proven its efficiency to promote vertical orientation of cylinder-forming PS-*b*-PEO thin films.[15] More recently, high temperature SVA, shortened by microwave annealing (μSVA), has also been developed. It ideally combines the attributes of SVA and thermal annealing with shorter annealing times, which is particularly suited for saccharide-based BCPs such as polystyrene-*b*-maltoheptaose (PS-*b*-MH) due to the moderate thermal stability of the MH block.[33]

In the quest for miniaturization, there is a constant need for smaller phase-separated microdomains. However, reducing BCP domain spacing by decreasing N requires to increase the χ value to maintain microphase separation (χN >10.5 for di-BCPs). Such highly incompatible BCPs, also coined as high-χ BCPs, are able to reach sub_10 nm self-assembled microdomains.[34] For instance, Russell, Xu and coworkers reported the directed self-assembly

of a PS-*b*-P2VP (M_n = 19.5 kg mol^{-1}) thin film coated onto a faceted sapphire substrate into perpendicular P2VP cylinders with diameters of 7.3 nm and a lattice spacing of 17.4 nm.[35] Self-assembled lamellar microdomains of poly(cyclohexylethylene)-*b*-PMMA with a domain spacing of 9.0 nm have also been reported.[36] Among others, silicon-containing BCPs have also been developed due to their high χ parameters and naturally high etch contrast, an important feature to apply BCP thin films as lithographic templates.[37,38]

Polystyrene-*b*-maltoheptaose (PS-*b*-MH) is a hybrid high-χ BCP comprising a synthetic PS block and a natural oligosaccharide MH block. The strong incompatibility arising from the hydrophobic and hydrophilic imbalance between the PS and MH blocks, enhanced sterically by the rigid "rod-like" structure of the carbohydrate block, leads to sub_10 nm microdomains after SVA.[10,33,39-42] While MH is an abundant renewable resource, a significant feature of MH-based high-χ BCPs is their mild thermal and chemical degradation thus providing a versatile etch contrast. In previous studies, SVA[39-41] and microwave annealing[33] conditions afforded out-of-plane orientation of the PS-*b*-MH microdomains on silicon substrates. PS-*b*-MH thin films were also subjected to graphoepitaxy for nanolithography applications,[41] and were used as dielectric layer in transistor memory devices.[10,42]

Although the strong incompatibility between the blocks of high-χ BCPs enables to reach sub_10 nm microdomains, the long-range ordering and the control of the mesostructure orientation are more challenging than for classical BCPs as an important chemical incompatibility often induces an increased surface energy mismatch between the blocks. As opposed to PS-*b*-PMMA for which interfacial energies of the PS and PMMA blocks with air are similar at high temperatures,[5] thermal annealing alone cannot overcome the difference in surface energy for high-χ BCPs, thus resulting in preferential wetting of one block at the top interface. Several strategies have been recently developed to tune the top interface of high-χ BCP thin films in order to impart perpendicular orientation.[43,44] Willson and coworkers

have reported polarity-switching topcoats based on alternating copolymers spin-coated from aqueous solutions above high-χ BCP thin films. After thermal annealing, the polarity of the topcoats switches from hydrophilic to hydrophobic/neutral through ring-closure of the anhydride moieties.[45] These polarity-switching topcoats were applied to several silicon-containing high-χ BCP thin films, in combination with substrate modification and directed self-assembly, to promote laterally aligned perpendicular microdomains.[46] Fluorinated surface-active polymer (SAP) additives have been reported as an alternative strategy to decrease the surface energy difference between the blocks located at the top interface with air.[47,48] The SAP additives were added to the BCP solution and segregated to the top interface during deposition and annealing steps to form a neutral topcoat. In combination with cross-linked underlayers, fluorinated SAP additives were employed to control the orientation of PS-*b*-poly(methyl 5-methyl-2-oxo-1,3-dioxane-5-carboxylate) (PS-*b*-PMTC-Me) and PS-*b*-P2VP microdomains.

Herein, we report the use of a series of cross-linked underlayers and a single phase preferential fluorinated BCP SAP additive for directing the self-assembly of a cylinder-forming PS-*b*-MH (M_n = 5.7 kg mol^{-1}, f_{MH} = 0.16) in thin films. A library of statistical photo-cross-linkable copolymers with 10-30 mol% of a carbohydrate-based acrylamide (AGA), 10-90 mol% of 4-vinylbenzyl azide, and 10-90 mol% of styrene were synthesized to generate cross-linked mats enabling the modification of the wetting properties of silicon substrates. Besides, a partially fluorinated analogue of PS-*b*-MH (PS-*b*-MHF with *ca*. 14% of hydroxyl groups of the MH block substituted by trifluoropropionyl moieties) was synthesized and used as an SAP additive able to segregate at the top surface of out-of-plane PS-*b*-MH microdomains upon spin-coating and annealing steps. The SAP additive was designed to be phase-preferential, *i.e.* the PS and MHF blocks segregate at the top interface and register above the PS and MH domains of the cylinder-forming self-assembled thin film, respectively. The self-assembled BCP thin films resulting from interfacial tuning of one, the other or both

interfaces were investigated by atomic force microscopy (AFM) and Synchrotron grazing incidence small angle X-ray scattering (GISAXS) experiments and compared to pristine PS-*b*-MH and PS-*b*-MHF thin films on silicon substrates. By tuning one or both interfaces, the orientation of the HEX cylindrical structure could be controlled. Additionally, epitaxial order-order transitions from the HEX phase to either face-centered orthorhombic (FCO) or body-centered cubic (BCC) spheres could also be triggered by manipulation of the bottom interface without changing the volume fraction of the PS-*b*-MH blocks.

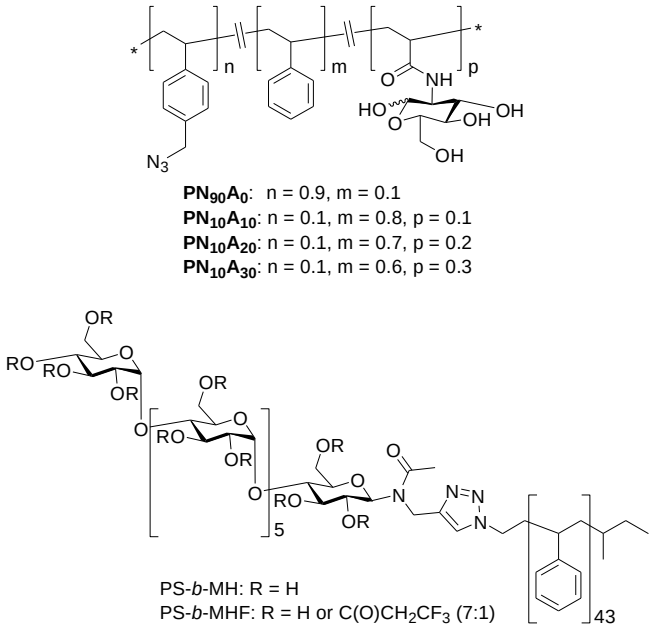

Figure 1. Chemical structures of cross-linkable statistical copolymers $\mathbf{PN_nA_p}$, cylinder-forming high-χ diblock copolymer PS-*b*-MH and partially fluorinated surface active diblock copolymer PS-*b*-MHF.

RESULTS AND DISCUSSION

Synthesis of Azide-Containing Photo-Cross-linkable Copolymers. Taking inspiration from earlier strategies to control the surface properties of planar substrates using cross-linked copolymer mats either made from comonomers representative of the BCP blocks,[27-30] or from a single monomer with varying amounts of a cross-linkable comonomer,[32] we have synthesized four different photo-cross-linkable statistical copolymers $\mathbf{PN_nA_p}$ (with *n* and *p* the mol% of 4-vinylbenzyl azide and AGA units, respectively, **Figure 1**). First, a PS-based

copolymer was obtained in two steps by RAFT copolymerization of *p*-chloromethyl styrene **1** and styrene **2** using **3** as chain transfer agent (CTA) followed by an azidation reaction in order to generate the photo-cross-linkable azidomethyl units. Copolymerizations were performed using a constant $[\mathbf{1} + \mathbf{2}]_0/[\mathbf{3}]_0/[\text{AIBN}]_0$ ratio of 300:1.0:0.5 and a $[\mathbf{1}]_0/[\mathbf{2}]_0$ ratio of 9:1 to obtain $\mathbf{PN_{90}A_0}$ in 65% yield with a number average polymerization degree (DP_n) of 195 (**Table 1**) and spectral data comparable to previously reported analogues.[49] A series of three photo-cross-linkable carbohydrate-containing statistical copolymers having 10 mol% of 4-vinylbenzyl azide and 10, 20 or 30 mol% of AGA **4** was then synthesized in two steps by CTA **3**-mediated RAFT copolymerization and subsequent azidation (**Figure S1** and **Table 1**). Copolymerizations were carried out using a constant $[\mathbf{1} + \mathbf{2} + \mathbf{4}]_0/[\mathbf{3}]_0/[\text{AIBN}]_0$ ratio of 400:1:0.5 and three comonomer fractions $[\mathbf{1}]_0/[\mathbf{2}]_0/[\mathbf{4}]_0$ of 1:8:1, 1:7:2 and 1:6:3. The RAFT copolymerizations for the syntheses of $\mathbf{PN_{10}A_{10}}$, $\mathbf{PN_{10}A_{20}}$ and $\mathbf{PN_{10}A_{30}}$ were stopped at low monomer conversions (*i.e.* below 25%) in order to limit the influence of composition drift (resulting from reactivity ratio differences) on the chains homogeneity. After 72 hours at 60 °C and purification by dialysis, azide-functionalized copolymers $\mathbf{PN_{10}A_{10}}$, $\mathbf{PN_{10}A_{20}}$ and $\mathbf{PN_{10}A_{30}}$ were obtained in 23, 15 and 11% yield and number average polymerization degrees (DP_n) of 90, 60 and 44, respectively.

The obtained copolymers were characterized by ATR-FTIR, SEC, ^{1}H and ^{13}C NMR spectroscopy. The intense stretching band of azide groups (2095 cm^{-1}), and the increasing intensity of the O-H/N-H stretching (3700-3100 cm^{-1}), C=O stretching (1650 cm^{-1}) and C-O stretching (1050 cm^{-1}) bands with the increase in AGA units are consistent with the targeted structures (**Figure S2**). The chemical structure of the copolymers was also confirmed by ^{1}H and ^{13}C NMR spectroscopy, as well as by distortionless enhanced polarization transfer (DEPT) and 2D ^{1}H-^{13}C heteronuclear single quantum coherence (HSQC) NMR spectroscopy (**Figure S3-S5**). As expected, ^{1}H NMR spectra in DMSO-d_6 demonstrated a constant signal of the azidomethylene protons at 4.3 ppm, a decrease of the signals of the styrenic units in the

7.5-6.7 ppm range and the concomitant increase of the signals due to the AGA units in the 5.5-3.0 ppm range when the AGA content increased from 10 to 30 mol% (**Figure S3**). The copolymers compositions were estimated by ^{1}H NMR from the integration of the aromatic, azidomethyl and anomeric protons by assuming a constant [**1**]/[**2**] molar ratio up to final conversions. All signals could be assigned using a combination of 1D (^{1}H and ^{13}C) and 2D (DEPT, HSQC) NMR spectroscopy (**Figure S4** and **S5**) for $\mathbf{PN_{10}A_{30}}$ that contains the highest molar fraction of AGA units. SEC analysis shows that the monomodal traces are shifted toward longer elution times (M_n decreases from 29.5 to 1.0 kg mol^{-1} according to PS standard) and exhibit higher chain dispersities ($Đ$ increases from 1.22 to 3.76) when the amount of AGA units increases from 0 to 30 mol% (**Figure S6**). The tailing and the shift to lower molar masses with increasing AGA content is most likely due to strong interactions of the AGA units with the stationary phase of the columns, also favored by chloroform as the eluent, and is thus over-expressed for high molar fractions of AGA units.

Reactivity ratios of styrene **2** (r_{St}) and AGA **4** (r_{AGA}) were determined by *in situ* ^{1}H NMR kinetic studies at 60 °C in DMF-d_7 using the Jaack's method.[50] The obtained values (r_{St} = 0.84 and r_{AGA} = 0.53) are typical of a statistical copolymerization (**Figure S7-S12**). These reactivity ratios were used to model the distribution of styrene/4-vinylbenzyl azide and AGA as well as the dispersity of a total of 10 chains for copolymers $\mathbf{PN_{10}A_{10}}$, $\mathbf{PN_{10}A_{20}}$ and $\mathbf{PN_{10}A_{30}}$ using the predictive program based on the Mayo-Lewis equation and Monte Carlo method developed by Xu and coworkers.[51] The calculations assumed identical reactivity ratios for styrene and 4-vinylbenzyl azide, and were based on their relative molar fractions in the monomer feed, the theoretical DP_n at 100% conversion and the experimental conversion determined by gravimetry. In fair accordance with the composition diagrams (**Figure S11** and **S12**), these simulations of the chains composition provide a complementary visualization of the statistical nature of the obtained copolymers (**Figure 2**).

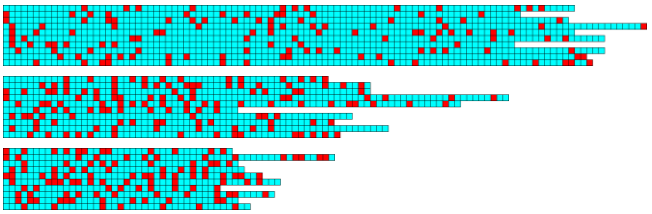

Figure 2. Simulation of the distribution of styrene/4-vinylbenzyl azide (blue squares) and AGA (red squares) units among ten different chains for $\mathbf{PN_{10}A_{10}}$ (top), $\mathbf{PN_{10}A_{20}}$ (middle) and $\mathbf{PN_{10}A_{30}}$ (bottom) with a targeted DP_n of 400 and monomer conversions of 23, 15 and 11%, respectively.[51] Each row represents a polymer chain.

Table 1. Properties of cross-linkable statistical copolymers $\mathbf{PN_nA_p}$.

Statistical copolymer	[**1**]/[**2**]/[**4**][a]	x [%][b]	DP_n[c]	M_n[d] [kg mol^{-1}]	$Đ$[d]
$\mathbf{PN_{90}A_0}$	0.9:0.1:0	65	195	26.5	1.22
$\mathbf{PN_{10}A_{10}}$	0.1:0.7:0.2	23	90	2.9	3.18
$\mathbf{PN_{10}A_{20}}$	0.1:0.6:0.3	15	60	1.5	3.55
$\mathbf{PN_{10}A_{30}}$	0.1:0.5:0.4	11	44	1.0	3.76

a) Estimated by ^{1}H NMR; b) Monomers conversion determined by gravimetry; c) Number average polymerization degrees obtained from the gravimetric conversion and monomers/CTA molar ratios in the feed; d) Determined by SEC in $CHCl_3$, according to PS standards.

Synthesis of Partially Fluorinated PS-*b*-MHF. A partially fluorinated analogue of PS-*b*-MH was synthesized as SAP additive for the modification of the outmost interface of PS-*b*-MH thin films through interfacial segregation during the spin-coating and annealing steps.[47,48] The SAP additive should ideally (i) migrate at the top interface to lower the surface energy thus preventing the formation of a wetting layer and (ii) promote the phase preferential selective registration of the SAP additive blocks with those of the BCP thin films to enhance out-of-plane orientation of the BCP microdomains throughout the film thickness. With that aim, the polysaccharide block of PS-*b*-MH was submitted to partial esterification using 0.14 equivalent of 3,3,3-trifluoropropionyl chloride **5** with respect to hydroxyl groups (*i.e. ca.* 3 fluorinated groups per MH block, **Figure S13**). PS-*b*-MHF was characterized by

ATR-FTIR, ^{1}H and ^{19}F NMR spectroscopy (**Figure S14-S16**). Besides a broadening of the signals of the polysaccharide block due to the lower solubility of PS-*b*-MHF compared to PS-*b*-MH in DMF, ^{1}H NMR of PS-*b*-MHF demonstrated a slight increase of the integrals corresponding to the signals in the 6.0-4.5 ppm range due to the increased number of protons from the CH_2CF_3 groups (**Figure S14**). ^{19}F NMR (**Figure S15**) highlighted the presence of the characteristic signals of CF_3 groups and showed that the esterification reaction occurs predominantly on the C6 position of the saccharidic units (δ ~ –63 ppm) due to the higher reactivity of primary alcohols. It is worth noting that secondary alcohols (C2 and C3, δ ~ –56 ppm) and to a smaller extent terminal alcohol (C4, δ ~ –53 ppm) can also be esterified. Besides, the decrease of the O-H stretching band (at 3300 cm^{-1}), the appearance of the C=O stretching band (at 1750 cm^{-1}) and the concomitant appearance of the C-F stretching band (at 1250 cm^{-1}) in the ATR-FTIR spectra of PS-*b*-MH and PS-*b*-MHF corroborates the occurrence of the esterification reaction (**Figure S16**).

Elaboration and Characterization of Cross-linked Underlayers. Cross-linked underlayers were prepared by spin-coating dilute solutions of azide-functionalized copolymers $\mathbf{PN_nA_p}$ (0.4–1.6 mg mL^{-1}) in 2:1 (v/v) mixtures of THF and PGMEA onto cleaned silicon substrates and subsequent photo-cross-linking under UV irradiation through the generation of highly reactive nitrene intermediates. After a 10 min annealing at 180 °C to ensure the total consumption of any remaining azide groups and evaporation of any residual solvent, the resulting coatings were fully insoluble in good solvents of the initial copolymers thus proving effective cross-linking which is a prerequisite to the subsequent spin coating of the PS-*b*-MH thin films. For all studied copolymers, the thickness of the cross-linked mats increased with the polymer concentration in the spin-coating solution (**Figure S17**). In order to minimize the thickness of the cross-linked mat without compromising the effectiveness of the substrate neutralization,[27,52] the thickness was fixed at *ca.* 15 nm by using 0.4 mg mL^{-1} solutions of the photo-cross-linkable precursors in 2:1 (v/v) mixtures of THF and PGMEA.

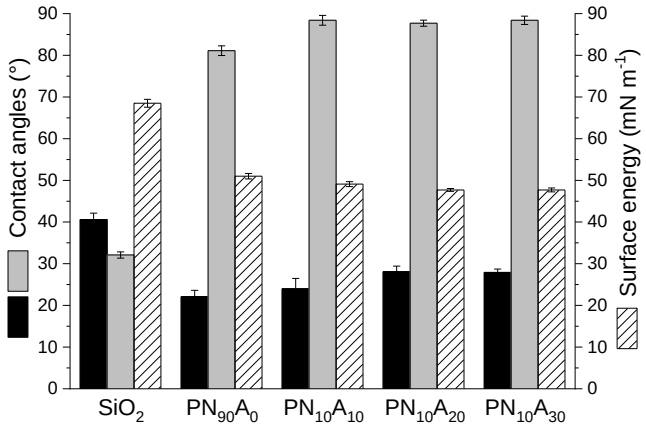

Figure 3. Contact angles of diiodomethane (black columns) and water (grey columns) on silicon substrates and on silicon substrates having *ca*. 15-nm-thick cross-linked mats of **$PN_{90}A_0$**, **$PN_{10}A_{10}$**, **$PN_{10}A_{20}$** and **$PN_{10}A_{30}$** (from left to right), and the corresponding surface energies (dashed columns). Error bars show mean standard deviations.

Contact angles were measured by the sessile drop method with water and diiodomethane as wetting liquids and the surface energies were determined using the Owens-Wendt-Rabel-Kaelbel method. Contact angle values were $\theta = 32°$ and $\theta = 81$-$88°$ for water and $\theta = 41°$ and θ = 22–28° for diiodomethane for the neat silicon wafer and the different cross-linked underlayers, respectively (**Figure 3**, **Table S1**). The surface energy (γ) of the silicon wafers was 68.5 mN m^{-1} while γ values for all cross-linked underlayers were in the 48–51 mN m^{-1} range. Surprisingly, the surface energies of the cross-linked underlayers are very similar whatever the content of AGA or azide units in the copolymer precursors. This suggests that the polar sugar units are expelled from the surface of the cross-linked films and that hydrophobic segments mostly contribute to the wetting properties and surface energies of the cross-linked coatings. In contrast, compared to sugar-containing underlayers the sugar-free and azide-rich **$PN_{90}A_0$** underlayer displays a lower water contact angle (θ = 88° and 81°, respectively) and a slightly higher surface energy (γ = 48–49 and 51 mN m^{-1}, respectively) demonstrating that the surface hydrophobicity of cross-linked underlayers is mainly guided by the chemical nature of the backbone of the polymer precursors.

Self-Assembly of PS-*b*-MH Thin Films with Finely Tuned Interfacial Properties. The self-assembly of cylinder-forming PS-*b*-MH was investigated by AFM and Synchrotron GISAXS using 15 different combinations of substrate chemical modifications and/or different contents of PS-*b*-MHF SAP additive (**Table S2**). A first series of five samples consists of PS-*b*-MH thin films supported on substrates with varying chemical nature. **SiO_2F_0**, the reference sample, is a PS-*b*-MH thin film coated on a pristine silicon substrate. **$PN_{90}A_0F_0$**, **$PN_{10}A_{10}F_0$**, **$PN_{10}A_{20}F_0$** and **$PN_{10}A_{30}F_0$** are PS-*b*-MH thin films of comparable thickness coated on cross-linked underlayers of distinct composition (*i.e.* 0, 10, 20 or 30 mol% of AGA units for **$PN_{90}A_0$**, **$PN_{10}A_{10}$**, **$PN_{10}A_{20}$** and **$PN_{10}A_{30}$**, respectively). Second, self-assembled PS-*b*-MH thin films containing 0, 10 or 20 wt% of PS-*b*-MHF SAP additive coated on silicon substrates (*i.e.* **SiO_2F_0**, **SiO_2F_{10}**, and **SiO_2F_{20}**, respectively) were compared to investigate the impact of the partially-fluorinated SAP additive. Finally, a last series (*i.e.* **$PN_{90}A_0F_{10}$**, **$PN_{90}A_0F_{20}$**, **$PN_{10}A_{10}F_{10}$**, **$PN_{10}A_{10}F_{20}$**, **$PN_{10}A_{20}F_{10}$**, **$PN_{10}A_{20}F_{20}$**, **$PN_{10}A_{30}F_{10}$** and **$PN_{10}A_{30}F_{20}$**) compares the self-assembly of PS-*b*-MH thin films combining both the modification of the bottom interface by cross-linked underlayers and the addition of 10 or 20 wt% of SAP additive. All cross-linked underlayers were 15 nm thick while PS-*b*-MH, PS-*b*-MHF and PS-*b*-MH/PS-*b*-MHF thin films were 30 nm thick.

Prior to morphological characterization, all samples were annealed by μSVA at 160 °C for 5 s in the presence of a 3:1 w/w THF/H_2O mixture, since THF and H_2O are good solvents of the PS and MH blocks, respectively. The morphologies of the PS-*b*-MH and PS-*b*-MH/PS-*b*-MHF thin films were carefully investigated by a combination of AFM and GISAXS experiments. The AFM phase images, the GISAXS 2D patterns and the GISAXS intensity cuts of all samples, as well as a detailed and comprehensive treatment of the GISAXS data are given in the ESI (**Figure S18-S38**).

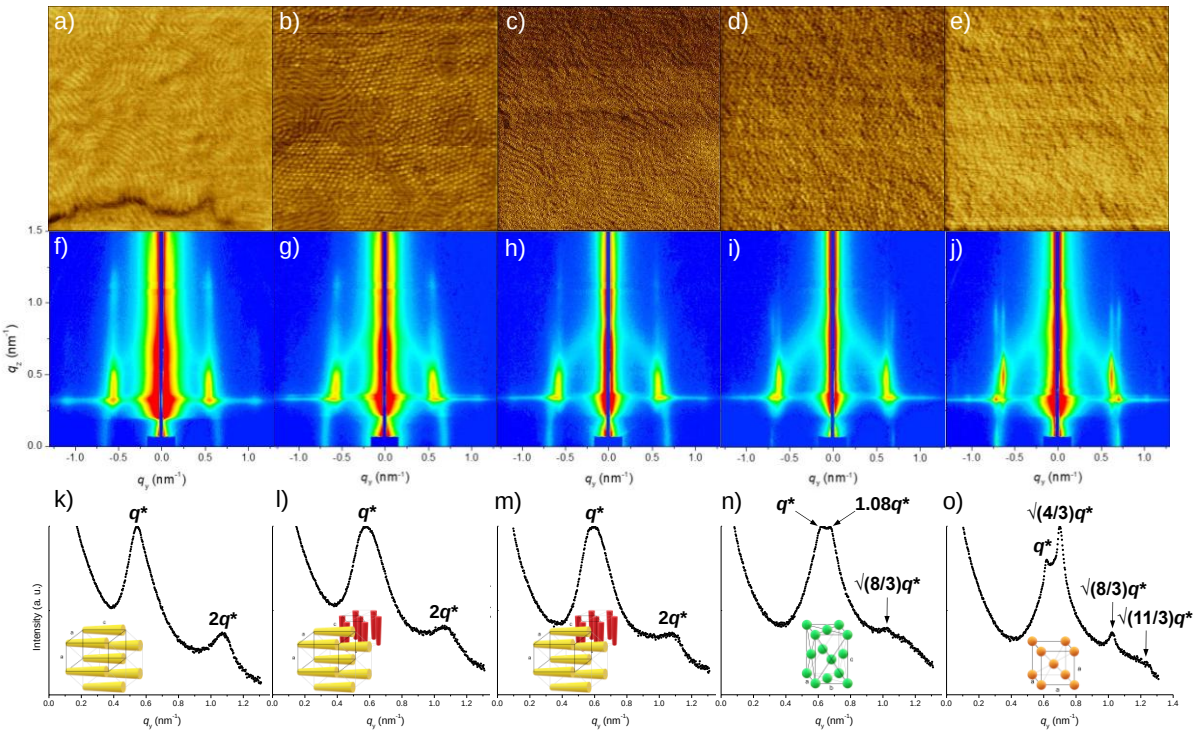

Figure 4. Effect of the cross-linked underlayer composition on the self-assembly of PS-*b*-MH thin films. (a-e) AFM phase images (500 nm × 500 nm), (f-j) 2D GISAXS patterns, (k-o) GISAXS intensity cuts along the horizontal q_y direction taken around the Yoneda band for (a,f,k) **SiO_2F_0**, (b,g,l) **$PN_{90}A_0F_0$**, (c,h,m) **$PN_{10}A_{10}F_0$**, (d,i,n) **$PN_{10}A_{20}F_0$**, and (e,j,o) and **$PN_{10}A_{30}F_0$**.

2.5. Self-Assembly of PS-*b*-MH Thin Films Supported on Cross-linked Underlayers

The AFM phase images and GISAXS patterns of **SiO_2F_0**, **$PN_{90}A_0F_0$**, **$PN_{10}A_{10}F_0$**, **$PN_{10}A_{20}F_0$** and **$PN_{10}A_{30}F_0$** are gathered in **Figure 4**. The AFM image of **SiO_2F_0** exhibits a fingerprint phase-separated structure typical of in-plane HEX cylinders (**Figure 4a**). This assignation is corroborated by the GISAXS intensity cuts along q_y showing a 1:2 relative peak position ratio from the primary scattering peak $q_y^* \sim 0.55$ nm^{-1} (**Figure 4k**). Additionally, the positions of the transmitted and reflected Bragg spots along q_z taken at $q_y^* \sim 0.55$ nm^{-1} are in accordance with the calculated positions expected for in-plane cylinders (see **Figure S19**). The AFM images of **$PN_{90}A_0F_0$** and **$PN_{10}A_{10}F_0$** also exhibit fingerprint phase-separated patterns related to in-plane HEX cylindrical structures even if this organization seems to co-exist with a population of out-of-plane cylinders (**Figure 4b,c**). This is corroborated by the

GISAXS intensity cuts along q_y showing: (i) a 1:2 relative peak position ratio from the primary scattering peak $q_y^* \sim 0.55$ nm^{-1} in accordance with an in-plane cylindrical structure, and (ii) a shoulder in the primary scattering peak at $q^* \sim 0.62$ nm^{-1}, coherent with the presence of a minor population of perpendicular cylinders as $q^{*\perp^{HEX}} \times \sqrt{3}/2 = q^{*//^{HEX}}$ (**Figure 4l,m**).[53] **$PN_{10}A_{20}F_0$** and **$PN_{10}A_{30}F_0$** display strikingly different AFM images and GISAXS patterns. Indeed, AFM phase images display a dot pattern which is difficult to undoubtedly assign to either cylindrical or spherical morphologies (**Figure 4d,e**). For **$PN_{10}A_{20}F_0$** the GISAXS intensity profile along q_y integrated around the Yoneda band exhibits a 1:1.08:$\sqrt{(8/3)}$ relative peak position ratio from $q_y^* \sim 0.62$ nm^{-1}, which is typical of a FCO arrangement of spheres (**Figure 4n**).[54,55] Conversely, for **$PN_{10}A_{30}F_0$** the relative peak position ratio obtained from the GISAXS intensity profile along q_y integrated around the Yoneda band is 1:$\sqrt{(4/3)}$:$\sqrt{(8/3)}$:$\sqrt{(11/3)}$ with $q_y^* \sim 0.62$ nm^{-1} in accordance with a BCC arrangement of spheres (**Figure 4o**).[56] These results demonstrate the occurrence of epitaxial order-order transitions (*i.e.* HEX parallel cylinders -> FCO spheres -> BCC spheres) induced by the distinct chemical nature of the cross-linked underlayers. Such epitaxial morphological transitions can only occur if there is (i) a matching parallel orientation of the cylinder axis and the [111] direction of the BCC lattice, and thus (ii) a match between the (110) *d*-spacing of the BCC lattice (d_{110}^{BCC}) and the (100) *d*-spacing of the HEX lattice (d_{100}^{HEX}).[57-60] In this series of samples, we experimentally obtained the required orientational match and a comparable *d*-spacing match ($d_{110}^{BCC} = 1.1 \times d_{100}^{HEX}$), as previously observed.[60] Since the PS-*b*-MH film thickness and the annealing conditions are identical, the different morphologies highlighted by GISAXS and the resulting epitaxial order-order transitions must be directly related to the different composition, physical and chemical properties of the cross-linked underlayers. In particular, the varying content of AGA units in the underlayers and the most likely distinct cross-link density might: (i) modify the amount of solvent trapped in the cross-linked underlayers after the spin-coating steps of the cross-linkable copolymers and the

BCPs,[61,62] (ii) modify the swelling of the cross-linked underlayers by the solvent mixture used for μSVA during the μSVA process, (iii) modify the interpenetration depth between PS-*b*-MH chains and the cross-linked underlayers,[63] (iv) induce a preferential interaction of the MH block with the underlayer, and/or (v) induce the consequent formation of a MH wetting layer able to shift the stability window of the BCP structure towards morphologies characterized by a lower volume fraction of MH (*i.e.* spheres).

Similar order-order transitions from cylinders to spheres in PS-*b*-MH thin films have been previously observed experimentally.[39,64] For instance, Aissou *et al*. demonstrated that in SiO_2-supported PS-*b*-MH thin films, hydrogen bonding between the hydroxyl groups of the MH block and bipyridine additive increased the volume fraction of the MH block and decreased the χN product owing to a moderation of the hydrophilic character of the MH/bipyridine block leading to the stabilization of a spherical structure.[39] Besides, by varying the THF/H_2O ratio from 1:1 to 1:0 during SVA, Liao *et al*. showed a transition from distorted HEX cylinders to face-centered cubic spheres in thin films of PS-*b*-MH supported by silicon substrates.[64] In the present work, it is unlikely that the different cross-linked underlayers modify the incompatibility parameter of PS-*b*-MH and thus the observed morphological changes are mostly related to interfacial phenomena triggered by the cross-linked mats. Nevertheless, although the chemical nature of the cross-linked underlayers has a significant impact on the morphology of PS-*b*-MH thin films, they are not able to efficiently promote the desired perpendicular cylindrical morphology. This is in strong contrast to *e.g.* the self-assembly of cylinder-forming PS-*b*-PMMA thin films where the chemical composition of the underlayers affords the control of the orientation of the PMMA cylinders without any change of morphology. These initial results on cross-linked underlayers further hints the need to precisely adjust the interfacial energy at the top interface to promote the formation of out-of-plane microdomains of PS-*b*-MH.[27-32]

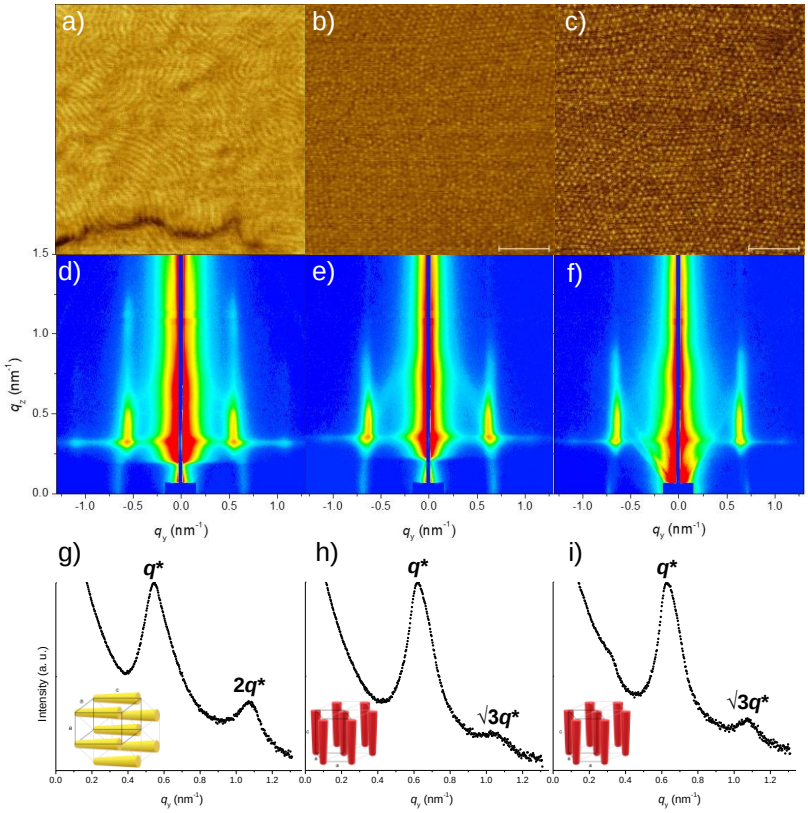

Figure 5. Effect of the content of PS-*b*-MHF SAP additive on the self-assembly of PS-*b*-MH thin films supported on silicon substrates. (a-c) AFM phase images (500 nm × 500 nm), (d-f) 2D GISAXS patterns, (g-i) GISAXS intensity cuts along the horizontal q_y direction taken around the Yoneda band for (a,d,g) **SiO_2F_0**, (b,e,h) **SiO_2F_{10}**, and (c,f,i) **SiO_2F_{20}**.

Self-Assembly of PS-*b*-MH Thin Films with Different Contents of PS-*b*-MHF SAP Additive. The AFM phase images and GISAXS patterns of **SiO_2F_0**, **SiO_2F_{10}**, and **SiO_2F_{20}** are featured on **Figure 5**. Conversely to **SiO_2F_0** (**Figure 5a**) and regardless of the content of SAP additive, the AFM images of **SiO_2F_{10}**, and **SiO_2F_{20}** display a dot pattern which could be either attributed to out-of-plane HEX cylinders or spheres (**Figure 5b,c**). The analysis of the GISAXS patterns and intensity cuts unambiguously demonstrates the presence of out-of-plane HEX cylinders with a 1:√3 relative peak position ratio obtained from the intensity cut along q_y with $q_y^* \sim 0.60$ nm^{-1} (**Figure 5h,i**). The formation of a topcoat layer resulting from the interfacial segregation of the PS-*b*-MHF SAP additive able to balance the surface energy mismatch at the top interface is most likely responsible for the orientation switch from in-plane to out-of-plane HEX cylinders. Additionally, the sharper scattering profile and the

higher scattering intensity of the $\sqrt{3}q^*$ peak for **SiO_2F_{20}** hint towards a better organization of the out-of-plan HEX cylinders as compared to **SiO_2F_{10}**. Since the PS-*b*-MH films are 30 nm thick and assuming a quantitative migration at the outermost interface, it is expected that the loading of 10 and 20 wt% of SAP additive affords *ca*. 3 and 6 nm thick topcoats, respectively. The improved ordering in **SiO_2F_{20}** is most likely related to a more homogenous coverage of the PS-*b*-MH thin film by the PS-*b*-MHF top-coat layer.[48] Note that higher loading of the SAP additive has not been investigated in this study, since we would expect an important modification of the self-assembly behavior of the blended PS-*b*-MH/PS-*b*-MHF layer through a phase separation mechanism highly influenced by the PS-*b*-MHF chains.

Different systems have demonstrated the controlled orientation of high-χ BCP microdomains using SAP additives. For instance, Zhang *et al.* have designed a BCP SAP additive (*i.e.* poly(methyl methacrylate)-*b*-poly(hexafluoroisopropyl methacrylate)) that combines a neutral block and a surface anchoring block.[48] The PMMA block matches surface tensions with respect to the underneath high-χ BCP domains while the low surface energy fluorinated block promotes the segregation of the SAP additive at the top interface. Another SAP system proposed by Vora *et al*. is based on the selective segregation of a low surface energy poly(hexafluoroalcohol styrene) at the top interface of poly(methyl 5-methyl-2-oxo-1,3-dioxane-5-carboxylate) thin films to balance the BCP/air interfacial energy, thus leading to an out-of-plane lamellar structure.[47] Herein, the PS-*b*-MHF SAP additive is directly derived from the PS-*b*-MH BCP. Although it shares the samecharacteristic dimensions as the PS-*b*-MH BCP, PS-*b*-MHF is not able to generate well-defined microdomains on silicon substrates after applying μSVA conditions used herein (see **Figure S38**). However, the blending of PS-*b*-MHF with the cylinder-forming PS-*b*-MH BCP leads to a registration at the top interface of the PS and MHF domains (due to the low surface energy of the MHF component) above the respective PS and MH domains (**Figure 6**).[65] This selective segregation behavior promotes the stabilization of HEX perpendicular cylinders as

attested by GISAXS (**Figure 5e,f,h,i**) and supported by the direct observation of the BCP pattern by AFM without resorting to preliminary plasma etching as in previous systems involving SAP additives (**Figure 5b,c**).

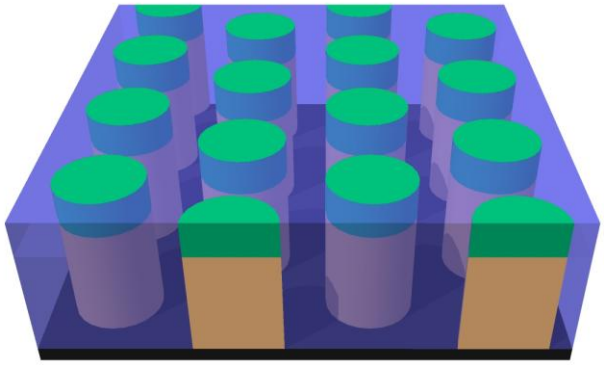

Figure 6. Registration of the phase-preferential PS-*b*-MHF SAP additive at the top interface of HEX perpendicular PS-*b*-MH cylinders.

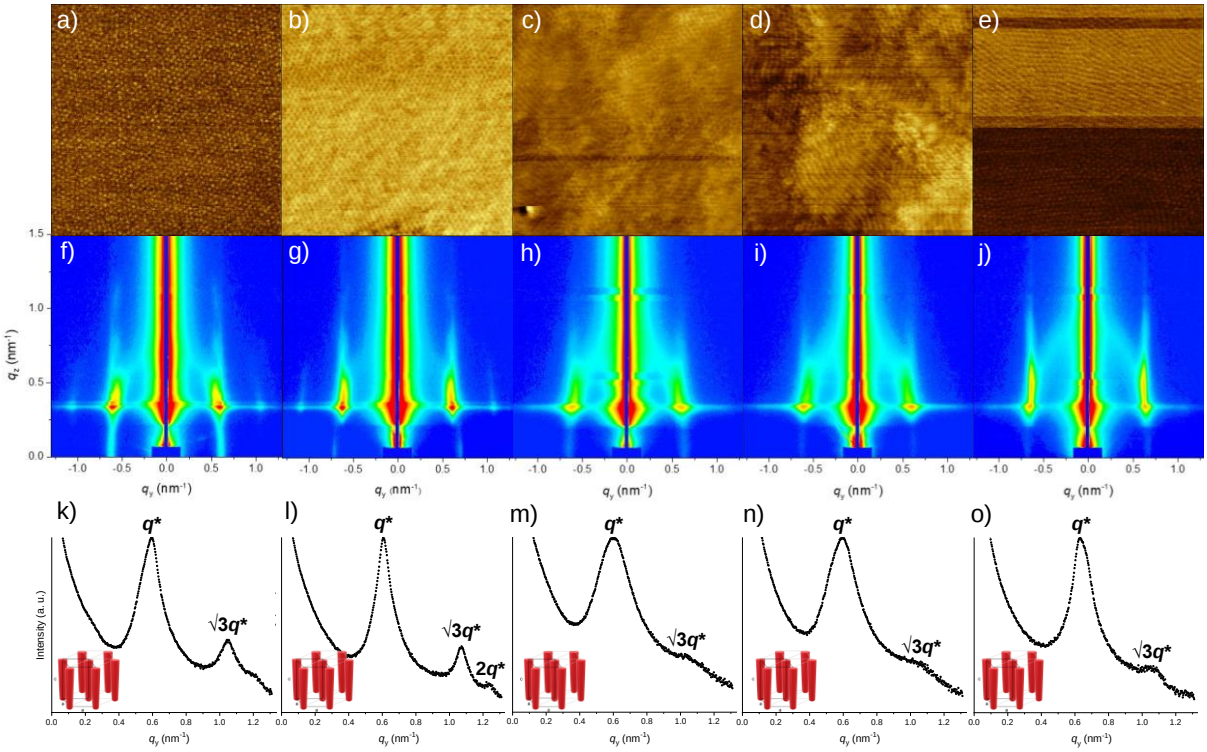

Figure 7. Combined effect of the cross-linked underlayer composition and PS-*b*-MHF SAP additive content on the self-assembly of PS-*b*-MH thin films. (a-e) AFM phase images (500 nm ×500 nm), (f-j) 2D GISAXS patterns, (k-o) GISAXS intensity cuts along the horizontal q_y

direction taken around the Yoneda band for (a,f,k) **$PN_{90}A_0F_{10}$**, (b,g,l) **$PN_{90}A_0F_{20}$**, (c,h,m) **$PN_{10}A_{10}F_{10}$**, (d,i,n) **$PN_{10}A_{10}F_{20}$**, and (e,j,o) and **$PN_{10}A_{20}F_{10}$**.

Self-Assembly of PS-*b*-MH Thin Films Supported on Different Underlayers with Various Contents of PS-*b*-MHF SAP Additive. As for PS-*b*-MH thin films casted on silicon substrates (*i.e.* **SiO_2F_0**, **SiO_2F_{10}**, and **SiO_2F_{20}**), a switch from in-plane HEX cylinders to out-of-plane HEX cylinders is observed for PS-*b*-MH thin films supported on **$PN_{90}A_0$** or **$PN_{10}A_{10}$** cross-linked underlayers when 10 or 20 wt% of PS-*b*-MHF SAP additive is incorporated (*i.e.* **$PN_{90}A_0F_{10}$**, **$PN_{90}A_0F_{20}$**, **$PN_{10}A_{10}F_{10}$**, and **$PN_{10}A_{10}F_{20}$** on **Figure 5**). Interestingly, sharper GISAXS patterns with the presence of higher order peaks were recorded for **$PN_{90}A_0F_{10}$**, **$PN_{90}A_0F_{20}$** which indicate a better translational ordering of the HEX structure (**Figure 7k,l**). However, although the SAP additive modifies the cylindrical structures with respect to **$PN_{10}A_{10}F_0$**, ill-ordered perpendicular cylinders with signatures of mixed orientation were observed for **$PN_{10}A_{10}F_{10}$**, and **$PN_{10}A_{10}F_{20}$** as attested by the broader and lower intensity peaks as well as the absence of high order peaks on the GISAXS q_y cuts (**Figure 7m,n**). As discussed above, for the highest content of AGA units the spherical morphology observed **$PN_{10}A_{30}F_0$** is maintained for both contents of the PS-*b*-MHF SAP additive in samples **$PN_{10}A_{30}F_{10}$** and **$PN_{10}A_{30}F_{20}$** (**Figure S34 and S37 in the ESI**), even though it is difficult to unambiguously attribute a FCO spherical structure to **$PN_{10}A_{30}F_{10}$**. The preferential interaction between the MH block and the cross-linked layer, which is responsible to the apparent shift of composition of the PS-*b*-MH towards the spherical window, may prevent the migration of the SAP at the top interface by trapping it within the spherical MH/MHF domains. Finally, a transition from FCO spheres (**$PN_{10}A_{20}F_0$**) to moderately well-ordered HEX perpendicular cylinders is observed for the combination of a **$PN_{10}A_{20}$** cross-linked underlayer with 10 wt% of PS-*b*-MH SAP additive (**$PN_{10}A_{20}F_{10}$**) as highlighted by the GISAXS q_y cut (**Figure 7o**) with a $\sqrt{3}q^*$ peak more intense than for **$PN_{10}A_{10}F_{10}$**, and **$PN_{10}A_{10}F_{20}$** (**Figure 7m,n**) but showing less order than for **$PN_{90}A_0F_{10}$** and **$PN_{90}A_0F_{20}$** (**Figure 7k,l**). Increase to 20 wt% of

PS-*b*-MH SAP additive (**$PN_{10}A_{20}F_{20}$**) does not further improve the control over the orientation as an ill-defined structure containing a majority of in-plane HEX cylinders is observed (**Figure S31 in the ESI**). As discussed previously, the presence of AGA in the **$PN_{10}A_{10}$**, **$PN_{10}A_{20}$** and **$PN_{10}A_{30}$** underlayers might induce the formation of a MH wetting layer that lowers the volume fraction of MH and thus shifts the PS-*b*-MH structures from cylindrical towards spherical morphologies. Extended segregation of the MH chains at this particular interface is expected for cross-linked underlayers with higher AGA content which in turn greatly influences the action of the SAP additive. It is worth mentioning that the presence of the cross-linked underlayers or the addition of the partially-fluorinated SAP additive did not significantly modify the lattice period or *d*-spacing values, defined by $d = 2\pi / q^*$. Indeed, while the reference sample **SiO_2F_0** has a *d* value of 11.4 nm, the slight variations observed for the other samples (*d* = 9.9-10.8 nm) are mainly related to the different morphologies and orientations observed (see **Table S3**).

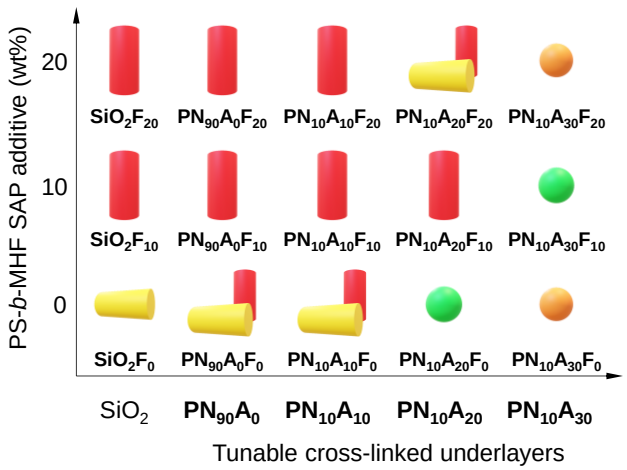

Figure 8. Morphology diagram of self-assembled PS-*b*-MH thin-films as a function of the substrate and PS-*b*-MHF SAP additive content. Red cylinders represent out-of-plane HEX cylinders morphology, yellow cylinders represent in-plane HEX cylinders morphology, green spheres represent FCO spheres morphology, orange spheres represent BCC spheres morphology.

CONCLUSIONS

This work demonstrates the efficient and versatile tuning of the morphology and orientation of the self-assembled microdomains of high-χ PS-*b*-MH thin films by controlling their interfacial properties using cross-linked underlayers of distinct composition and/or a phase-preferential partially-fluorinated PS-*b*-MHF SAP additive. To do so we have synthesized a library of cross-linkable statistical copolymers with different contents of photo-cross-linkable azide and AGA units. The influence of the chemical/physical properties of the cross-linked underlayers on the self-assembly of PS-*b*-MH thin films was demonstrated. While HEX in-plane cylinders are obtained on silicon substrates, epitaxial order-order transitions to HEX out-of-plane cylinders, as well as FCO and BCC spheres are observed when the amount of AGA units in the cross-linked underlayers was increased from 0 to 30 mol%. Despite having comparable wetting properties, the distinct composition of the cross-linked underlayers is most likely responsible for the different morphologies and orientations observed for PS-*b*-MH thin films. Besides, a phase-preferential PS-*b*-MHF SAP additive designed to segregate at the top interface of PS-*b*-MH thin films and reduce the surface energy of the MH block was shown to induce an orientation switch of PS-*b*-MH thin films from HEX in-plane cylinders to HEX out-of-plane cylinders. Finally, the interplay between different cross-linked underlayers and various amounts of PS-*b*-MHF SAP additive on the self-assembly of PS-*b*-MH thin films was investigated. The ability of the SAP additive to segregate at the top interface was described, depending on the composition of the underlayer and the self-assembly promoted by the underlayer. In particular, it was highlighted that the combination of a highly cross-linked underlayer and an SAP additive resulted in a better ordering of HEX perpendicular cylinders than employing the SAP additive on silicon substrates. However, in the presence of SAP additive, the introduction of AGA units in the cross-linked underlayers proved to be detrimental to the self-assembly into HEX out-of-plane cylinders. Therefore, several self-assembled nanostructures with distinct orientations and morphologies could be obtained in

thin film by simply tuning the interfacial properties of a single cylinder-forming PS-*b*-MH (**Figure 8**). Several combinations of cross-linked underlayer and SAP additive allowed the formation of HEX out-of-plane cylinders, which have the desired perpendicular orientation required for many applications in the field of nanotechnologies. We believe that the order of these HEX perpendicular cylinders could be further optimized. Additional studies regarding the self-assembly of PS-*b*-MH with (i) a cross-linked underlayer of poly(4-vinylbenzyl azide) homopolymer, (ii) cross-linked underlayers and BCP of different thicknesses and/or (iii) further loading of the SAP additive to screen the effects of cross-linking density, embedded solvent and segregation at the top interface, are currently undergoing. Another perspective is to further investigate the extent of orientational control provided for thicker films, for which the interfacial fields produced by the cross-linked mats and the SAP additive are expected to decrease with increasing BCP film thickness. The μSVA conditions for the self-assembly of pure PS-*b*-MHF and PS-*b*-MH/PS-*b*-MHF thin films should also be investigated. Finally, this general strategy relying on the control of top and bottom interfaces in PS-*b*-MH thin films could be advantageously extended to other relevant high-χ BCPs.

EXPERIMENTAL SECTION

Nomenclature. The nomenclature used for the cross-linkable statistical copolymers is as follows: $\mathbf{PN_nA_p}$, where *n* and *p* indicate the molar percentages of azide and carbohydrate groups, respectively. The molar percentage *m* of styrene in the polymerization medium is thus implicitly given by $m = 100 - (n + p)$. The nomenclature used for self-assembled thin-films is as follows: $\mathbf{PN_nA_pF_q}$, for thin films deposited on cross-linked underlayers $\mathbf{PN_nA_p}$, where *n* and *p* indicate the molar percentage of azide and carbohydrate groups, respectively, and *q* the percentage of PS-*b*-MHF in the thin-film (*q* = 0, 10, 20 or 100%). $\mathbf{SiO_2F_q}$, for thin films deposited on pristine silicon substrates, where *q* indicates the percentage of PS-*b*-MHF in the thin-film (*q* = 0, 10, 20 or 100%).

Materials. 4-Vinylbenzyl chloride (**1**, 90%), styrene (**2**, >99%), 2-(dodecylthiocarbonothioylthio)-2-methylpropionic acid (**3**, 98%), 2,2′-azobis(2-methylpropionitrile) (AIBN, 98%), sodium azide (NaN_3, 99.5%) and propylene glycol monomethyl ether acetate (PGMEA, 99.5%) were purchased from Merck. **1** and **2** were passed through a short column of basic alumina to remove the inhibitor. The synthesis of glucosamine acryloyl (AGA, **4**),[66] and polystyrene-*b*-maltoheptaose (PS-*b*-MH, M_n = 5.7 kg mol^{-1}, ϕ_{MH} = 0.16, $Đ$ = 1.05),[39] were described elsewhere. Cross-linkable azide-functionalized polystyrene $\mathbf{PN_{90}A_0}$ was synthesized as previously reported.[49] 3,3,3-Trifluoropropionyl chloride (**5**, 98%) was purchased from FluoroChem and used as received. Silicon wafers (500–550 μm thick with a native oxide layer of ca. 1–2 nm) were purchased from Siltronix (France). The silicon substrates were cut into approximatively 2 × 2 cm^2 pieces, treated by oxygen plasma during 15 min and rinsed with THF before use.

Nuclear Magnetic Resonance. ^{1}H (500 MHz), ^{13}C (125 MHz) and ^{19}F (375 MHz) NMR spectra were recorded on a Bruker Avance 500 spectrometer. Chemical shifts are reported in part per million (δ, ppm) relative to hydrogenated solvent residual peaks (^{1}H: δ = 7.26 ppm for $CHCl_3$, δ = 2.50 ppm for DMSO, δ = 8.03 ppm for DMF; ^{13}C: δ = 77.16 ppm for $CHCl_3$, δ = 39.52 ppm for DMSO). Abbreviations for peak multiplicity are given as follows: s for singlet, d for doublet, t for triplet, m for multiplet and b for broad.

Size Exclusion Chromatography. Size exclusion chromatography (SEC) experiments were carried out in chloroform at 22 °C and at a flow rate of 1.0 mL min^{-1} using a system equipped with a Shimadzu RI-10A Refractometer, an Agilent PLgel 5μm MIXED-C Column (300 × 7.5 mm) and an Agilent PLgel μm Guard pre-column (50 × 7.5 mm). Chloroform solutions of the cross-linkable statistical copolymers at 4 mg mL^{-1} were filtered through poly(tetrafluoroethylene) (PTFE) filters with 0.45 μm pore size. M_n values and chain dispersities $Đ$ were calculated using a calibration curve obtained from polystyrene standards.

FTIR Analysis. FTIR analyses were carried out using a Thermo Scientific Nicolet iS10 FTIR spectrometer equipped with a Smart iTR ATR accessory at a resolution of 4 cm^{-1}. A small quantity of cross-linkable statistical copolymers was deposited on the ATR diamond. Transmitted $I(\nu)$ and incident $I_0(\nu)$ beam energies were converted into a spectrum in absorbance A using the ATR correction: $A(\nu) = -(\nu/1000) \times \log[I(\nu)/I_0(\nu)]$ where ν is the wavenumber in cm^{-1}.

General Procedure for Reversible Addition-Fragmentation Chain Transfer (RAFT) Copolymerization, Synthesis of $PN_{10}A_{10}$. A solution of **1** (288 mg, 1.70 mmol), **2** (1.41 g, 13.6 mmol), **3** (15.5 mg, 4.25×10^{-2} mmol), **4** (396 mg, 1.70 mmol) and AIBN (3.4 mg, 2.1×10^{-2} mmol) in DMF (8.6 mL) was transferred into a glass ampule which was thoroughly deoxygenated by three freeze–pump–thaw cycles and sealed under vacuum. The solution was heated at 60 °C for 72 h. The crude mixture was then transferred into a round bottom flask and NaN_3 (221 mg, 3.40 mmol) was added. The solution was stirred overnight at 45 °C and then introduced into a dialysis membrane (Spectra/Por from Spectrum Labs with a molar mass cut-off of 3.5 kg mol^{-1}). It was then successively dialyzed against *ca.* 500 mL of DMSO, EtOH/DMSO 1:1 (v/v), EtOH, EtOH/H_2O 1:1 (v/v) and finally H_2O under gentle stirring at room temperature during at least 6 h each. Solvents or solvent mixtures were renewed every 3h. The resulting precipitated solid was recovered, freeze-dried and $\mathbf{PN_{10}A_{10}}$ was obtained as a slightly orange powder (487 mg, $DP_n = 90$, $x = 23$ %, $M_n = 29.4$ kg mol^{-1} eq PS, $Đ = 3.1$). ^{1}H NMR (500 MHz, DMSO-d_6, δ): 7.52-6.77 (5H, b, $\mathbf{H}_d$, $\mathbf{H}_{f'}$), 6.75-5.85 (5H, b, $\mathbf{H}_e$, $\mathbf{H}_i$), 4.94 (1H, b, $\mathbf{H}_{k\alpha}$), 4.44 (1H, b, $\mathbf{H}_{k\beta}$), 4.29 (2H, s, $\mathbf{H}_g$), 3.79-2.98 (6H, bm, $\mathbf{H}_j$, $\mathbf{H}_l$, $\mathbf{H}_m$, $\mathbf{H}_n$, $\mathbf{H}_o$), 2.40-0.62 (9H, bm, $\mathbf{H}_a$, $\mathbf{H}_{a'}$, $\mathbf{H}_b$, $\mathbf{H}_{b'}$).

Synthesis of $PN_{10}A_{20}$. The general procedure for RAFT copolymerization was applied to **1** (127 mg, 0.75 mmol), **2** (546 mg, 5.25 mmol), **3** (6.8 mg, 1.9×10^{-2} mmol), **4** (349 mg, 1.50 mmol), AIBN (1.5 mg, 9.4×10^{-3} mmol), DMF (4.1 mL) and NaN_3 (97.5 mg, 1.50 mmol) to

obtain **$PN_{10}A_{20}$** as a slightly orange powder (150 mg, x = 15 %, DP_n = 60, M_n = 15.2 kg mol^{-1} eq PS, $Đ$ = 3.5). ^{1}H NMR (500 MHz, DMSO-d_6, δ): 7.52-6.77 (5H, b, $\mathbf{H}_d$, $\mathbf{H}_{f'}$), 6.75-5.85 (5H, b, $\mathbf{H}_e$, $\mathbf{H}_i$), 4.94 (1H, b, $\mathbf{H}_{k\alpha}$), 4.44 (1H, b, $\mathbf{H}_{k\beta}$), 4.29 (2H, s, $\mathbf{H}_g$), 3.79-2.98 (6H, bm, $\mathbf{H}_j$, $\mathbf{H}_l$, $\mathbf{H}_m$, $\mathbf{H}_n$, $\mathbf{H}_o$), 2.40-0.62 (9H, bm, $\mathbf{H}_a$, $\mathbf{H}_{a'}$, $\mathbf{H}_b$, $\mathbf{H}_{b'}$).

Synthesis of $PN_{10}A_{30}$. The general procedure for RAFT copolymerization was applied to **1** (144 mg, 0.85 mmol), **2** (530 mg, 5.10 mmol), **3** (7.8 mg, 2.1 × 10^{-2} mmol), **4** (594 mg, 2.55 mmol), AIBN (1.7 mg, 1.1 × 10^{-2} mmol), DMF (5.1 mL) and NaN_3 (111 mg, 1.70 mmol) to obtain **$PN_{10}A_{30}$** as a slightly orange powder (144 mg, x = 11 %, DP_n = 44, M_n = 10.4 kg mol^{-1} eq PS, $Đ$ = 3.7). ^{1}H NMR (500 MHz, DMSO-d_6, δ) 7.52-6.77 (5H, b, $\mathbf{H}_d$, $\mathbf{H}_{f'}$), 6.75-5.85 (5H, b, $\mathbf{H}_e$, $\mathbf{H}_i$), 4.94 (1H, b, $\mathbf{H}_{k\alpha}$), 4.44 (1H, b, $\mathbf{H}_{k\beta}$), 4.29 (2H, s, $\mathbf{H}_g$), 3.79-2.98 (6H, bm, $\mathbf{H}_j$, $\mathbf{H}_l$, $\mathbf{H}_m$, $\mathbf{H}_n$, $\mathbf{H}_o$), 2.40-0.62 (9H, bm, $\mathbf{H}_a$, $\mathbf{H}_{a'}$, $\mathbf{H}_b$, $\mathbf{H}_{b'}$); ^{13}C NMR (125 MHz, DMSO-d_6, δ): 174.71 (1C, $\mathbf{C}_h$), 144.90 (2C, $\mathbf{C}_c$), 132.75 (1C, $\mathbf{C}_f$), 128.72-124.96 (5C, $\mathbf{C}_d$, $\mathbf{C}_e$, $\mathbf{C}_{f'}$), 96.34 (1C, $\mathbf{C}_{k\beta}$), 90.71 (1C, $\mathbf{C}_{k\alpha}$), 76.37-53.51 (4C, $\mathbf{C}_j$, $\mathbf{C}_l$, $\mathbf{C}_n$, $\mathbf{C}_o$,), 61.65 (1C, $\mathbf{C}_m$), 53.51 (1C, $\mathbf{C}_g$), 49.96-40.41 (4C, $\mathbf{C}_a$, $\mathbf{C}_{a'}$, $\mathbf{C}_b$, $\mathbf{C}_{b'}$).

Synthesis of PS-b-MHF. A solution of PS-*b*-MH (1.00 g, 3.96 mmol of hydroxyl groups) in anhydrous pyridine (10 mL) in a flame dried flask equipped with magnetic stirrer was maintained at 0 °C and **5** (54 µL, 0.53 mmol) was added. The reaction was slowly allowed to reach room temperature and left overnight. The solvent was removed under vacuum and the crude product was dissolved in a small amount of THF and precipitated in methanol to remove the residual salts and remaining pyridine. After drying at 45 °C in an oven overnight, a brownish-yellow powder of partially fluorinated PS-*b*-MHF was obtained (1.0 g, 93 %). ^{1}H NMR (500 MHz, DMF-d_7, δ): 7.90-7.71(1H, m, $\mathbf{H}_j$), 7.61-6.92 (3H, b, $\mathbf{H}_i$, $\mathbf{H}_g$), 6.92-6.37 (2H, bm, $\mathbf{H}_h$), 6.12-3.18 (10H, bm, O**H**, $\mathbf{H}_l$, $\mathbf{H}_k$, $\mathbf{H}_m$, $\mathbf{H}_n$, $\mathbf{H}_o$, $\mathbf{H}_p$, $\mathbf{H}_q$, C$\mathbf{H}_2$CF_3), 2.47-1.16 (3H, bm, $\mathbf{H}_e$, $\mathbf{H}_f$), 1.16-0.54 (9H, bm, $\mathbf{H}_a$, $\mathbf{H}_b$, $\mathbf{H}_c$, $\mathbf{H}_d$); ^{19}F NMR (375 MHz, DMF-d_7, δ): –52.56 (3F,

C4C(O)OCH$_2$C**F**$_3$), –55.42, –56.98 (3F, C2C(O)OCH$_2$C**F**$_3$, C3C(O)OCH$_2$C**F**$_3$), –62.85, –63.80 (3F, C6C(O)OCH$_2$C**F**$_3$).

Spin-coating. Spin-coating of the cross-linkable statistical copolymers, and BCP solutions was performed using a Polos Spin 150 apparatus. The processing parameters for each sample are detailed further below.

Cross-linking. Cross-linking of the underlayers was performed using a Hönle UVA Cube 400 equipped with a UV lamp. Samples were placed at 12 cm from the UV light source and irradiated for 30 min. They were afterward annealed at 180 °C for 10 min to ensure total consumption of azide groups and evaporation of any residual solvent.

Microwave annealing. Microwave annealing (μSVA) was performed with a Biotage Initiator 2.5 microwave synthesizer equipped with an infrared sensor (accuracy: 5 °C). The annealing solvent mixture (0.7 mL THF/H_2O 3:1 w/w) was introduced into microwave reaction vials (0.5–2 mL type, Biotage).[33] A glass support was put inside of the reaction vial as a sample holder during the annealing process. The vial was then sealed with a cap after placing a spin-coated sample on the top of the sample holder. The solvent mixture inside the vial was heated with 2.45 GHz microwave energy to reach the targeted temperature. The heating process took approximately few minutes. The targeted temperature of 160 °C was kept for an annealing time of 5 s with the help of the temperature feedback-control system of the microwave synthesizer. The vial was then cooled down to 45 °C with air flow. The output microwave power, the temperature of the vial and the pressure inside of the vial were recorded by the microwave synthesizer.

General Procedure for the Preparation of Cross-linked Thin Films, Thin Film of $PN_{10}A_{10}$. Solutions of $PN_{10}A_{10}$ at 0.4–1.6 mg mL^{-1} were prepared in a mixture of THF/PGMEA 2:1 (v/v), stirred and filtered through 0.45 μm PTFE filters. The solution was spin-coated at 4000 rpm for 30 s followed by 15 s at 6000 rpm. After drying under ambient conditions the films were cross-linked under UV irradiation for 30 min followed by a 10 min

annealing at 180 °C. Cross-linking efficiency was controlled by recovery of the initial film thickness after dipping the substrate into THF. The same process was applied to photo-cross-linkable analogues **$PN_{10}A_{20}$**, **$PN_{10}A_{30}$** and **$PN_{90}A_{0}$**.

Thin Films of PS-b-MH. A solution of PS-*b*-MH at 1.2 mg mL^{-1} was prepared in anisole, stirred, and filtered through 0.45 µm PTFE filters. The solution was spin-coated at 2000 rpm for 30 s using either pristine silicon substrates or silicon substrates covered with *ca.* 15 nm thick cross-linked underlayers of **$PN_{90}A_{0}$**, **$PN_{10}A_{10}$**, **$PN_{10}A_{20}$** and **$PN_{10}A_{30}$**. The films were dried in the air prior to microwave annealing with 0.7 mL THF/H_2O 3:1 w/w at 160 °C for 5 s.

Thin Films of PS-b-MH with PS-b-MHF SAP additive. PS-*b*-MH and PS-*b*-MHF (9:1 and 8:2 w/w) were dissolved in anisole to afford 1.2 mg mL^{-1} solutions. The same processing conditions as for the preparation of thin films of PS-*b*-MH were then applied.

Reflectometry. Mean values of film thicknesses were measured using a Filmetrics F20-UV reflectometer, on at least ten different places on the sample.

Surface energy. Contact angle measurements were performed on the cross-linked underlayers using a Krüss Easy Drop DSA25 Goniometer with H_2O and diiodomethane (CH_2I_2) as sensing liquids. The sessile drop method was used with a volume of 1 µL and the given contact angle values were the mean of at least five different measurements at different places of the sample. The surface energies were then deduced from the Owens-Wendt-Rabel-Kaelbel (OWRK) method exploiting Young's equation (equation 1):

$$\gamma_S = \gamma_{SL} + \gamma_L cos\theta \quad (1)$$

with γ_S the surface free energy of the solid, γ_{SL} the interfacial tension between solid and liquid, γ_L the surface tension of the liquid and θ the contact angle. In the OWRK method, y_S and γ_L are split into a polar *p* and a dispersive *d* part (equations 2 and 3):

$$\gamma_S = \gamma_S^p + \gamma_S^d \quad (2)$$

$$\gamma_L = \gamma_L^p + \gamma_L^d \quad (3)$$

Surface energies were calculated using a single linear regression with both components of water and diiodomethane (γ_{H2O}^{p} = 51.0 mN m^{-1} and γ_{H2O}^{d} = 21.8 mN m^{-1}, γ_{CH2I2}^{p} = 1.3 mN m^{-1} and γ_{CH2I2}^{d} = 49.58 mN m^{-1}) combining equations 1 and 4:

$$\gamma_{SL} = \gamma_S + \gamma_L - 2(\sqrt{\gamma_S^d \gamma_L^d} + \sqrt{\gamma_S^p \gamma_L^p}) \quad (4)$$

Atomic Force Microscopy. Film surfaces were imaged by Atomic Force Microscopy (AFM) under ambient temperature in tapping mode with a Bruker Dimension Icon atomic force microscope. APP Nano silicon cantilevers with resonant frequencies of 200–400 kHz were used. Unless otherwise specified, 500 nm × 500 nm images were recorded.

Synchrotron Grazing Incidence Small Angle X-Ray Scattering. The GISAXS measurements were carried out at the NCD-SWEET Beamline at the ALBA Light Source Synchrotron (Spain). A beam energy of 12.4 keV (λ = 1 *Å*) was prepared using a Si (1 1 1) channel cut monochromator and further collimated using an array of Be lenses. The GISAXS 2D patterns were recorded using a Pilatus1M 3 S detector (Dectris®), which consists of a 981 × 1043 pixels array with a pixel size of 172 μm × 172 μm (H × V), recording and combining two images for filling the intrinsic horizontal detector gaps. The scattering vector q was calibrated using Silver Behenate as reference, obtaining a sample to detector distance of 4007 mm. The X-ray beam incident angle α_i was set at 0.18°, fully penetrating the polymer layer while minimizing the substrate signal. The scattering patterns were collected for 120 s to have an adequate signal to noise ratio. All the presented GISAXS patterns are zoomed-in views from larger patterns. The measured in-plane range was q_y = -1.3–1.3 nm^{-1} and out-of-plane range was q_z = -0.6–2.2 nm^{-1}. A detailed and comprehensive description of the GISAXS data is given in the Supporting Information.

ASSOCIATED CONTENT

Supporting Information

The Supporting Information is available free of charge at https://pubs.acs.org/doi/10.1021/acsami.xxxxxxx.

Detailed characterization of $\mathbf{PN_nA_p}$ statistical copolymers and PS-*b*-MHF SAP additive, determination of the reactivity ratios, evolution of the thickness of cross-linked underlayers as a function of concentration, high resolution AFM images and detailed analysis of GISAXS data (PDF).

AUTHOR INFORMATION

Corresponding Authors

Eric Drockenmuller – Univ Lyon, Université Lyon 1, CNRS, Ingénierie des Matériaux Polymères, UMR 5223, F-69003 Lyon, France; orcid.org/0000-0003-0575-279X; Email: eric.drockenmuller@univ-lyon.fr

Guillaume Fleury – Univ. Bordeaux, CNRS, Bordeaux INP, LCPO, UMR 5629, F-33600, Pessac, France; orcid.org/ 0000-0003-0779-191X; Email: guillaume.fleury@u-bordeaux.fr

Redouane Borsali – Univ Grenoble Alpes, CNRS, CERMAV, UPR 5301, F-38000 Grenoble, France; orcid.org/ 0000-0002-7245-586X; Email: redouane.borsali@cermav.cnrs.fr

Authors

Noémie Baumgarten – Univ Lyon, Université Lyon 1, CNRS, Ingénierie des Matériaux Polymères, UMR 5223, F-69003 Lyon, France; orcid.org/0000-0001-9409-1908

Muhammad Mumtaz – Université Grenoble Alpes, CNRS, Centre de Recherches sur les Macromolécules Végétales, UPR 5301, F-38000 Grenoble, France

Daniel Hermida Merino – Dutch-Belgian Beamline, Netherlands Organization for Scientific Research, European Synchrotron Radiation Facility, F-38000 Grenoble, France;

Departamento de Física Aplicada, CINBIO, Universidade de Vigo, Campus Lagoas-Marcosende, E36310 Vigo, Galicia, Spain; orcid.org/ 0000-0002-8181-158X

Eduardo Solano – NCD-SWEET Beamline, ALBA Synchrotron Light Source, 08290 Cerdanyola del Valles, Spain; orcid.org/0000-0002-2348-2271

Julien Bernard – Université de Lyon, CNRS, Université Claude Bernard Lyon 1, INSA Lyon, Université Jean Monnet, UMR 5223, Ingénierie des Matériaux Polymères F-69621 Lyon Cédex, France; orcid.org/0000-0002-9969-1686

Sami Halila – Université Grenoble Alpes, CNRS, Centre de Recherches sur les Macromolécules Végétales, UPR 5301, F-38000 Grenoble, France; orcid.org/0000-0002-9673-1099

Complete contact information is available at: https://pubs.acs.org/doi/10.1021/acsami.xxxxxxx

Notes

The authors declare no competing financial interest.

Acknowledgements

The authors gratefully acknowledge the financial support from the ANR through the SWEETSURF project (ANR-17-CE09-0008). Partial financial support is acknowledged from the CNRS, Univ Grenoble Alpes and Univ Lyon.

REFERENCES

[1] Segalman, R. A. Patterning with Block Copolymer Thin Films. *Mater. Sci. Eng. R* **2005**, *48*, 191-226.

[2] Stoykovich, M. P.; Nealey, P. F. Block Copolymers and Conventional Lithography. *Materials Today* **2006**, *9*, 20-29.

[3] Cheng, J. Y.; Ross, C. A.; Smith, H. I.; Thomas, E. L. Templated Self-Assembly of

Block Copolymers: Top-Down Helps Bottom-Up. *Adv. Mater.* **2006**, *18*, 2505-2521.

[4] Bang, J.; Jeong, U.; Ryu, D. Y.; Russell, T. P.; Hawker, C. J. Block Copolymer Nanolithography: Translation of Molecular Level Control to Nanoscale Patterns. *Adv. Mater.* **2009**, *21*, 4769-4792.

[5] Bates, C. M.; Maher, M. J.; Janes, D. W.; Ellison, C. J.; Willson, C. G. Block Copolymer Lithography. *Macromolecules* **2014**, *47*, 2-12.

[6] Black, C. T.; Ruiz, R.; Breyta, G.; Cheng, J. Y. Colburn, M. E.; Guarini, K. W.; Kim, H.-C.; Zhang, Y. Polymer Self-Assembly in Semiconductor Microelectronics. *IBM J. Res. & Dev.* **2007**, *51*, 605-633.

[7] Morris, M. A. Directed Self-Assembly of Block Copolymers for Nanocircuitry Fabrication. *Microelectron. Eng.* **2015**, *132*, 207-217.

[8] Albrecht, T. R.; Bedau, D.; Dobisz, E.; Gao, H.; Grobis, M.; Hellwig, O.; Kercher, D.; Lille, J.; Marinero, E.; Patel, K.; Ruiz, R.; Schabes, M. E.; Wan, L.; Weller, D.; Wu, T.-S. Bit Patterned Media at 1 Tdot/in^2 and Beyond. *IEEE Transactions on Magnetics* **2013**, *49*, 773-778.

[9] Jung, Y. S.; Ross, C. A.; Well-Ordered Thin-Film Nanopore Arrays Formed Using a Block Copolymer Template. *Small* **2009**, *5*, 1654-1659.

[10] Chuang, T.-H.; Chiang, Y.-C.; Hsieh, H.-C.; Isono, T.; Huang, C.-W.; Borsali, R.; Satoh, T.; Chen, W.-C. Nanostructure- and Orientation-Controlled Resistive Memory Behaviors of Carbohydrate-*block*-Polystyrene with Different Molecular Weights via Solvent Annealing. *ACS Appl. Mater. Interfaces* **2020**, *12*, 23217-23224.

[11] Hampu, N.; Werber, J. R.; Chan, W. Y.; Feinberg, E. C.; Hillmyer, M. A. Next-Generation Ultrafiltration Membranes Enabled by Block Copolymers. *ACS Nano* **2020**, *14*, 16446-16471.

[12] Guo, C.; Lin, Y.-H.; Witman, M. D.; Smith, K. A.; Wang, C.; Hexemer, A.; Strzalka, J.; Gomez, E. D.; Verduzco, R. Conjugated Block Copolymer Photovoltaics with near 3% Efficiency through Microphase Separation. *Nano Lett.* **2013**, *13*, 2957-2963.

[13] Song, D.-P.; Jacucci, G.; Dundar, F.; Naik, A.; Fei, H.-H.; Vignolini, S.; Watkins, J. J. Photonic Resins: Designing Optical Appearance via Block Copolymer Self-Assembly. *Macromolecules* **2018**, *51*, 2395-2400.

[14] Russell, T. P.; Chai, Y. 50th Anniversary Perspective: Putting the Squeeze in Polymers: A Perspective on Polymer Thin Films and Interfaces. *Macromolecules* **2017**, *50*, 4597-4609.

[15] Sinturel, C.; Vayer, M.; Morris, M.; Hillmyer, M. A. Solvent Vapor Annealing of

Block Polymer Thin Films. *Macromolecules* **2013**, *46*, 5399-5415.

[16] Majewski, P. W.; Yager, K. G. Rapid Ordering of Block Copolymer Thin Films. *J. Phys.: Condens. Matter* **2016**, *28*, 403002.

[17] Segalman, R. A.; Yokoyama, H.; Kramer, E. J. Graphoepitaxy of Spherical Domain Block Copolymer Films. *Adv. Mater.* **2001**, *13*, 1152-1155.

[18] Yang, J. K. W.; Jung, Y. S.; Chang, J.-B.; Mickiewicz, R. A.; Alexander-Katz, A.; Ross, C. A. Complex Self-Assembled Patterns Using Sparse Commensurate Templates with Locally Varying Motifs. *Nat. Nanotechnol.* **2010**, *5*, 256-260.

[19] Angelescu, D. E.; Waller, J. H.; Adamson, D. H.; Deshpande, P.; Chou, S. Y.; Register, R. A.; Chaikin, P. M. Macroscopic Orientation of Block Copolymer Cylinders in Single-Layer Films by Shearing. *Adv. Mater.* **2004**, *16*, 1736-1740.

[20] Morkved, T. L.; Lu, M.; Urbas, A. M.; Ehrichs, E. E.; Jaeger, H. M.; Mansky, P.; Russell, T. P. Local Control of Microdomain Orientation in Diblock Copolymer Thin Films with Electric Fields. *Science* **1996**, *273*, 931-933.

[21] De Rosa, C.; Park, C.; Thomas, E. L.; Lotz, B. Microdomain Patterns from Directional Eutectic Solidification and Epitaxy. *Nature* **2000**, *405*, 433-437.

[22] Mansky, P.; Liu, Y.; Huang, E.; Russell, T. P.; Hawker, C. Controlling Polymer-Surface Interactions with Random Copolymer Brushes. *Science* **1997**, *275*, 1458-1460.

[23] Ji, S.; Liu, G.; Zheng, F.; Craig, G. S. W.; Himpsel, F. J.; Nealey, P. F. Preparation of Neutral Wetting Brushes for Block Copolymer Films from Homopolymer Blends. *Adv. Mater.* **2008**, *20*, 3054-3060.

[24] In, I.; La, Y.-H.; Park, S.-M.; Nealey, P. F.; Gopalan, P. Side-Chain-Grafted Random Copolymer Brushes as Neutral Surfaces for Controlling the Orientation of Block Copolymer Microdomains in Thin Films. *Langmuir* **2006**, *22*, 7855-7860.

[25] She, M.-S.; Lo, T.-Y.; Ho, R.-M. Long-Range Ordering of Block Copolymer Cylinders Driven by Combining Thermal Annealing and Substrate Functionalization. *ACS Nano* **2013**, *7*, 2000-2011.

[26] Gu, W.; Hong, S. W.; Russell, T. P. Orienting Block Copolymer Microdomains with Block Copolymer Brushes. *ACS Nano* **2012**, *11*, 10250-10257.

[27] Ryu, D. Y.; Shin, K; Drockenmuller, E.; Hawker, C. J.; Russell, T. P.; A Generalized Approach to the Modification of Solid Surfaces. *Science* **2005**, *308*, 236-239.

[28] Bang, J.; Bae, J.; Löwenhielm, P.; Spiessberger, C.; Given-Beck, S. A.; Russell, T. P.; Hawker, C. J. Facile Routes to Patterned Surface Neutralization Layers for Block Copolymer Lithography. *Adv. Mater.* **2007**, *19*, 4552-4557.

[29] Han, E.; In, I.; Park, S.-M.; La, Y.-H.; Wang, Y.; Nealey, P. F.; Gopalan, P. Photo-patternable Imaging Layers for Controlling Block Copolymer Microdomain Orientation. *Adv. Mater.* **2007**, *19*, 4448-4452.

[30] Jung, H.; Leibfarth, F. A.; Woo, S.; Lee, S.; Kang, M.; Moon, B.; Hawker, C. J.; Bang, J. Efficient Surface Neutralization and Enhanced Substrate Adhesion Through Ketene Mediated Cross-Linking and Functionalization. *Adv. Func. Mater* **2013**, *23*, 1597-1602.

[31] Sun, Y.-S.; Wang, C.-T.; Liou, J.-Y. Tuning Polymer-Surface Chemistries and Interfacial Interactions with UV irradiated Polystyrene Chains to Control Domain Orientations in Thin Films of PS-b-PMMA. *Soft Matter* **2016**, *12*, 2923.

[32] Bates, C. M.; Strahan, J. R.; Santos, L. J.; Mueller, B. K.; Bamgbade, B. O.; Lee, J. A; Katzenstein, J. M.; Ellison, C. J.; Willson, C. J. Polymeric Cross-Linked Surface Treatments for Controlling Block Copolymer Orientation in Thin Films. *Langmuir* **2011**, *27*, 2000-2006.

[33] Liao, Y.; Chen, W.-C.; Borsali, R. Carbohydrate-Based Block Copolymer Thin Films: Ultrafast Nano-Organization with 7 nm Resolution Using Microwave Energy. *Adv. Mater.* **2017**, *29*, 1701645.

[34] Sinturel, C.; Bates, F. S.; Hillmyer, M. A. High-χ–Low N Block Polymers: How Far Can We Go? *ACS Macro Lett.* **2015**, *4*, 1044-1050.

[35] Park, S.; Lee, D. H.; Xu, J.; Kim, B.; Hong, S. W.; Jeong, U.; Xu, T.; Russell, T. P. Macroscopic 10-Terabit-per-Square-Inch Arrays from Block Copolymers with Lateral Order. *Science* **2009**, *323*, 1030-1033.

[36] Kennemur, J. G.; Yao, L.; Bates, F. S.; Hillmyer, M. A. Sub-5 nm Domains in Ordered Poly(Cyclohexylethylene)-*block*-poly(methyl methacrylate) Block Polymers for Lithography. *Macromolecules* **2014**, *47*, 1411-1418.

[37] Durand, W. J.; Blachut, G.; Maher, M. J.; Sirard, S.; Tein, S.; Carlson, M. C.; Asano, Y.; Zhou, S. X.; Lane, A. P.; Bates, C. M.; Ellison, C. J.; Willson, C. G. Design of High-χ Block Copolymers for Lithography. *Journal of Polymer Science, Part A: Polymer Chemistry* **2015**, *53*, 344-352.

[38] Matsunaga, K.; Kukai, W.; Ishizaki, M.; Kurihara, M.; Yamamoto, S.; Mitsuishi, M.; Yabu, H.; Nagano, S.; Matsui, J. Formation of Perpendicularly Aligned Sub-10 nm Nanocylinders in Poly(N-dodecylacrylamide-b-ethylene glycol) Block Copolymer Films by Hierarchical Phase Separation. *Macromolecules* **2020**, *53*, 9601-9610.

[39] Aissou, K.; Otsuka, I.; Rochas, C.; Fort, S.; Halila, S.; Borsali, R. Nano-Organization of Amylose-*b*-Polystyrene Block Copolymer Films Doped with Bipyridine. *Langmuir* **2011**, *27*, 4098-4108.

[40] Otsuka, I.; Tallegas, S.; Sakai, Y.; Rochas, C.; Halila, S.; Fort, S.; Bsiesy, A.; Baron, T.; Borsali, R. Control of 10 nm Scale Cylinder Orientation in Self-Organized Sugar-Based Block Copolymer Thin Films. *Nanoscale* **2013**, *5*, 2637-2641.

[41] Otsuka, I.; Nilsson, N.; Suyatin, D. B.; Maximov, I.; Borsali, R. Carbohydrate-Based Block Copolymer Systems: Directed Self-Assembly for Nanolithography Applications. *Soft Matter* **2017**, *13*, 7406-7411.

[42] Chiu, Y.-C.; Otsuka, I.; Halila, S.; Borsali, R.; Chen, W.-C. High-Performance Nonvolatile Transistor Memories of Pentacene Using the Green Electrets of Sugar-Based Block Copolymers and Their Supramolecules. *Adv. Func. Mater.* **2014**, *24*, 4240-4249.

[43] Suh, H. S.; Kim, D. H.; Moni, P.; Xiong, S.; Ocola, L. E.; Zaluzec, N. J.; Gleason, K. K.; Nealey P. F. Sub-10-nm patterning via directed self-assembly of block copolymer films with a vapour-phase deposited topcoat. *Nat. Nanotech.* **2017**, *12*, 575-581.

[44] Oh, J.; Suh, H. S.; Ko, Y.; Nah, Y.; Lee, J.-C.; Yeom, B.; Char, K.; Ross, C. A.; Son, J. G. Universal perpendicular orientation of block copolymer microdomains using filtered plasma. *Nat. Commun.* **2019**, *10*, 2912.

[45] Bates, C. M.; Seshimo, T.; Maher, M. J.; Durand, W. J.; Cushen, J. D.; Dean, L. M.; Blachut, G.; Ellison, C. J.; Willson, C. G. Polarity-Switching Top Coats Enable Orientation of Sub-10 nm Block Copolymer Domains. *Science* **2012**, *338*, 775-779.

[46] Maher, M. J.; Bates, C. M.; Blachut, G.; Sirard, S.; Self, J. L.; Carlson, M. C.; Dean, L. M.; Cushen, J. D.; Durand, W. J.; Hayes, C. O.; Ellison, C. J.; Willson, C. G. Interfacial Design for Block Copolymer Thin Films. *Chem. Mater.* **2014**, *26*, 1471-1479.

[47] Vora, A.; Schmidt, K.; Alva, G.; Arellano, N.; Magbitang, T.; Chunder, A.; Thompson, L. E.; Lofano, E.; Pitera, J. W.; Cheng, J. Y.; Sanders, D. P. Orientation Control of Block Copolymers using Surface Active, Phase-Preferential Additives. *ACS Appl. Mater. Interfaces* **2016**, *8*, 29808-29817.

[48] Zhang, J.; Clark, M. B.; Wu, C.; Li, M.; Trefonas III, P.; Hustad, P. D. Orientation Control in Thin Films of a High-X Block Copolymer with a Surface Active Embedded Neutral Layer. *Nano Lett.* **2016**, *16*, 728-735.

[49] Al Akhrass, S.; Gal, F.; Damiron, D.; Alcouffe, P.; Hawker, C. J.; Carrot, G.; Drockenmuller, E. Design of Crosslinked Hybrid Multilayer Thin Films from Azido-functionalized Polystyrenes and Platinum Nanoparticles. *Soft Matter* **2009**, *5*, 586-592.

[50] Jaacks, V. A Novel Method of Determination of Reactivity Ratios in Binary and Ternary Copolymerizations. *Die Makromolekulare Chemie* **1972**, *161*, 161-172.

[51] Smith, A. A. A.; Hall, A.; Wu, V.; Xu, T. Practical Prediction of Heteropolymer Composition and Drift. *ACS Macro Lett.* **2019**, *8*, 36-40.

[52] Ryu, D. Y.; Wang, J.-Y.; Lavery, K. A.; Drockenmuller, E.; Satija, S. K.; Hawker, C. J.; Russell, T. P. Surface Modification with Cross-Linked Random Copolymers: Minimum Effective Thickness. *Macromolecules* **2007**, *40*, 4296-4300.

[53] Lee, B.; Park, I.; Yoon, J.; Park, S.; Kim, J.; Kim, K.-W.; Chang, T.; Ree, M. Structural Analysis of Block Copolymer Thin Films with Grazing Incidence Small Angle X-Ray Scattering. *Macromolecules* **2005**, *38*, 4311-4323.

[54] Mishra, V.; Hur, S.; Cochran, E. W.; Stein, G. E.; Fredrickson, G. H.; Kramer, E. J. Symmetry Transition in Thin Films of Diblock Copolymer/Homopolymer Blends. *Macromolecules* **2010**, *43*, 1942-1949.

[55] Gunkel, I.; Gu, X.; Sun, Z.; Schaible, E.; Hexemer, A.; Russell, T. P. An *In Situ* GISAXS Study of Selective Solvent Vapor Annealing in Thin Block Copolymer Films: Symmetry Breaking of In-Plane Sphere Order upon Swelling. *Journal of Polymer Science, Part B: Polymer Physics* **2015**, *54*, 331-338.

[56] Stein, G. E.; Kramer, E. J.; Li, X.; Wang, J. Layering Transitions in Thin Films of Spherical-Domain Block Copolymers. *Macromolecules* **2007**, *40*, 2453-2460.

[57] Kimishima, K.; Saijo, K.; Koga, T.; Hashimoto, T. Time-Resolved High-Resolution SAXS Studies of OOT Process and Mechanism from Hex-Cylinder to BCC-Sphere in a Polystyrene-*block*-polyisoprene Diblock Copolymer. *Macromolecules* **2013**, *46*, 9032-9044.

[58] Sota, N.; Saito, K.; Hasegawa, H.; Hashimoto, T. Directed Self-Assembly of Block Copolymers into Twin BCC-Sphere: Phase Transition Process from Aligned Hex-Cylinder to BCC-Sphere Induced by a Temperature Jump between the Two Equilibrium Phases. *Macromolecules* **2013**, *46*, 2298-2316.

[59] Liao, F.; Shi, L.-Y.; Cheng, L.-C.; Lee, S.; Ran, R.; Yager, K. G.; Ross, C. A. Self-Assembly of a Silicon-Containing Side-Chain Liquid Crystalline Block Copolymer in Bulk and in Thin Films: Kinetic Pathway of a Cylinder to Sphere Transition. *Nanoscale* **2019**, *11*, 285-293.

[60] Matsen, M. W. Cylinder ↔ Sphere Epitaxial Transitions in Block Copolymer Melts. *J. Chem. Phys.* **2001**, *114*, 8165-8173.

[61] Seguini, G.; Zanenga, F.; Giammaria, T. J.; Ceresoli, M.; Sparnacci, K.; Antonioli, D.; Gianotti, V.; Laus, M.; Perego, M. Enhanced Lateral Ordering in Cylinder Forming PS-b-PMMA Block CopolymersExploiting the Entrapped Solvent. *ACS Appl. Mater. Interfaces* **2016**, *8*, 8280-8288.

[62] Sparnacci, K.; Chiarcos, R.; Gianotti, V.; Laus, M.; Giammaria, T. J.; Perego, M.; Munaò, G.; De Nicola, A.; Haese, M.; Kreuzer, L. P.; Widmann, T.; Müller-Buschbaum, P. Effect of Trapped Solvent on the Interface between PS-b-PMMA Thin Films and P(S-r-MMA) Brush Layers. *ACS Appl. Mater. Interfaces* **2020**, *12*, 7777-7787.

[63] Yang, W.-C.; Wu, S.-H.; Chen, Y.-F.; Nelson, A.; Wu, C.-M.; Sun, Y.-S. Effects of the Density of Chemical Cross-Links and Physical Entanglements of Ultraviolet-Irradiated Polystyrene Chains on Domain Orientation and Spatial Order of Polystyrene-block-Poly(methyl methacrylate) Nano-Domains. *Langmuir* **2019**, *35*, 14017-14030.

[64] Liao, Y.; Goujon, L. J.; Reynaud, E.; Halila, S.; Gibaud, A.; Wei, B.; Borsali, R. Self-Assembly of Copper-free Maltoheptaose-block-polystyrene Nanostructured Thin Films in Real and Reciprocal Space. *Carbohydr. Polym.* **2019**, *212*, 222-228.

[65] Kim, E.; Shin, C.; Ahn, H.; Ryu, D. Y.; Bang, J.; Hawker, C. J.; Russell, T. P. Size Control and Registration of Nano-Structured Thin Films by Cross-Linkable Units. *Soft Matter* **2008**, *4*, 475-479.

[66] Bernard, J.; Hao, X.; Davis, T. P.; Barner-Kowollik, C.; Stenzel, M. H. Synthesis of Various Glycopolymer Architectures via RAFT Polymerization: From Block Copolymers to Stars. *Biomacromolecules* **2006**, *7*, 232–238.

ToC figure

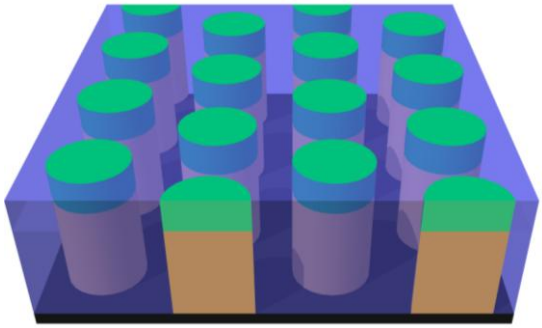

- Phase preferential SAP additive
- High-χ BCP
- Cross-linked passivation layer
- Tunable self-assembled microstructure